Dimensionality-controlled Mott transition and correlation effects in single-layer and bilayer perovskite iridates

Q. Wang, Y. Cao, J. A. Waugh, S. R. Park, T. F. Qi, O. B. Korneta, G. Cao, and D. S. Dessau

Phys. Rev. B **87**, 245109 — Published 13 June 2013

DOI: 10.1103/PhysRevB.87.245109

Dimensionality controlled Mott transition and correlation effects in single- and bi-layer perovskite iridates

Q. Wang,[1,2] Y. Cao,[1] J. A. Waugh,[1] S. R. Park,[1] T. F. Qi,[3] O. B. Korneta,[3] G. Cao,[3] and D. S. Dessau[1]

[1]*Department of Physics, University of Colorado, Boulder, CO 80309, USA*

[2]*Los Alamos National Laboratory, Los Alamos, NM 87545, USA*

[3]*Center for Advanced Materials, Department of Physics and Astronomy, University of Kentucky, Lexington, KY 40506, USA*

We studied Sr_2IrO_4 and $Sr_3Ir_2O_7$ using angle-resolved photoemission spectroscopy (ARPES), making direct experimental determinations of intra- and inter-cell coupling parameters as well as Mott correlations and gap sizes. The results are generally consistent with LDA+U+Spin-orbit coupling (SOC) calculations, though the calculations missed the momentum positions of the dominant electronic states and neglected the importance of inter-cell coupling on the size of the Mott gap. The calculations also ignore the correlation-induced spectral peak widths, which are critical for making a connection to activation energies determined from transport experiments. The data indicate a dimensionality-controlled Mott transition in these 5d transition-metal oxides (TMOs).

I. INTRODUCTION

Compared to the extensively studied 3d TMOs, such as high-T_c cuprate superconductors[1] in which the strong electron correlation plays a dominant role in determining the electronic structures, the 5d TMOs have several fundamental differences: the 5d electrons are more extended in real space which leads to a large band width and a reduced Coulomb correlation, and the very large atomic number leads to a large SOC effect. The delicate interplay between

electron correlations, SOC, inter-site hopping, and crystal field splitting leads to a strongly competing ground state for the 5d TMOs, including the iridates. So far, a great amount of exotic physics behaviors have been theoretically proposed to exist in the iridates, such as high-T_c superconductivity[2], quantum spin Hall and correlated topological insulator effects[3,4,5,6], and a Weyl Fermion state[7], though these are all currently lacking experimental verifications. Recently, the insulating behavior of single- and bi-layer perovskite strontium iridates Sr_2IrO_4 and $Sr_3Ir_2O_7$ has been explained by the cooperative interplay between correlation effects and strong SOC of the iridium 5d electrons[8,9,10,11,12,13]. The optical conductivity, ARPES, X-ray absorption spectroscopy, and resonant inelastic X-ray scattering[8,9,13] all appear consistent with these materials being classified as J_{eff}=1/2 Mott insulators, though a recent theoretical proposal[14] claimed that they are actually Slater insulators.

In this letter, we report a systematic ARPES study on single- and bi-layer perovskite iridates Sr_2IrO_4 and $Sr_3Ir_2O_7$. The band dispersions of both materials were mapped and compared to the available calculations. While the overall electronic structures of both materials appear roughly consistent with the LDA+U+SOC calculations based on the J_{eff}=1/2 Mott ground state picture, important differences remain. Specifically, we found the lowest energy (closest to E_F) states locate near the zone corner (X point), while they are theoretically predicted to be at the Γ point. This may be due to an underestimate of the SOC strength, or a strongly momentum-dependent electronic self-energy. An additional aspect missing from the calculations is the three-dimensional (3D) inter-cell coupling, which is significant (~ 100 meV) in $Sr_3Ir_2O_7$ and almost absent in Sr_2IrO_4. This inter-cell coupling appears to drive the reduction in the Mott gap, placing $Sr_3Ir_2O_7$ on the precipice of a Mott transition. Finally, the finite spectral peak widths are

completely ignored in the calculations and are argued to be highly relevant for making a connection to transport experiments as well as for predicting when the Mott transition may occur.

II. EXPERIMENTAL DETAILS

High-quality single crystals of Sr_2IrO_4 and $Sr_3Ir_2O_7$ were synthesized using a self-flux technique[15,16]. The crystals were cleaved in situ and measured in an ultra-high vacuum better than 3×10^{-11} torr. The ARPES experiments were performed at Beamline PGM-A (071) at the Synchrotron Radiation Center (SRC), Madison, and Beamline 7.0.1 at the Advanced Light Source (ALS), Berkeley. The angular resolution of the experiments was approximately 0.1^{o} and the energy resolution was 20 ~ 35 meV (depending upon photon energy).

III. RESULTS AND DISCUSSION

A. Experimental electronic structure

Fig. 1(a) shows the in-plane crystal structure of Sr_2IrO_4 and $Sr_3Ir_2O_7$. An important structural feature of these compounds is that they crystallize in a reduced tetragonal structure due to a rotation of the IrO_6-octahedra about the c-axis by ~ 11^{o}, resulting in a larger in-plane unit cell by $\sqrt{2} \times \sqrt{2}$ as shown as the red dashed box in the figure[17,18]. Figs. 1(b1)-1(b4) show the intensity maps of Sr_2IrO_4 at different binding energies from 0.1 eV to 0.4 eV. The white box in panel (b1) shows the first two-dimensional (2D) Brillouin zone (BZ) boundary with high symmetry points labeled. Consistent with its insulating behavior, there is no spectral weight at the Fermi level. Figs. 1(c1)-1(c5) show the spectra taken along the high symmetry directions over several BZs as indicated by the yellow cuts in panel (b1). Figs. 1(d1)-1(d5) are the second-derivative images along the energy direction of spectra (c1)-(c5), respectively, which enhances

the contrast of the raw spectra and makes it easier to track the electronic dispersion. The solid red lines are guides to the eye for the dispersions that can be resolved in the spectra, while the dashed red lines are guides to the eye for the dispersions that cannot be resolved in the specific spectra due to the matrix element effect[19,20] but do show up at the spectra taken along the same high symmetry direction but at different BZs. This dispersion data should be viewed as the centroids of spectral weight, as it is sometimes not possible for us to individually distinguish multiple bands that are close together. Figs. 2(a1)-2(a5) show the intensity maps of $Sr_3Ir_2O_7$ from the Fermi level to 0.4 eV. Compared to the single-layer material there is slightly more spectral weight at the Fermi level, which is principally due to the increased "leakage" of spectral weight up to the Fermi level due to the smaller gap of $Sr_3Ir_2O_7$. This leakage can be due to intrinsic correlation effects as well as the finite energy resolution of the experiment, and will be discussed again in conjunction with fig. 5. Figs. 2(b1)-2(b5) show the spectra taken along the high symmetry directions over several two-dimensional BZs as indicated by the yellow cuts in panel (a1). Similar to Sr_2IrO_4, there is no band crossing the Fermi level but the dispersions are much closer to the Fermi level. So the spectral weight shown in fig. 2(a1) rather indicates a smaller energy gap in $Sr_3Ir_2O_7$ than in Sr_2IrO_4. Figs. 2(c1)-2(c5) are the second-derivative images along the energy direction of spectra (b1)-(b5), respectively. Again, the solid and dashed lines in panels (c1)-(c5) are guides to the eye for the experimentally observed dispersions.

B. Comparison to theoretical calculations

Fig. 3 shows a compilation of the dispersion data for Sr_2IrO_4 and $Sr_3Ir_2O_7$, as well as a comparison to the LDA+U+SOC calculations adopted from S. J. Moon *et al*[9]. Figs. 3(b) and 3(d) are the experimentally extracted in-plane dispersions for both materials, which again should be viewed as the centroids of spectral weight. First of all, for both materials, there is no band

crossing the Fermi level, which is consistent with their insulating behavior. Compared to the single-layer compound, the uppermost band of bi-layer $Sr_3Ir_2O_7$ is much closer to the Fermi level. This is much clearer in figs. 3(e) and 3(f), which show stacks of EDCs along the Γ-X-Γ line for both materials. Furthermore, there are clearly more bands observed for $Sr_3Ir_2O_7$ in the same energy range, which is naturally explained as the bilayer splitting due to the intra-cell coupling. In particular, the bilayer splitting is observed to be minimum at the X point and maximum at the Γ point, with magnitude about 0.25 eV.

Fig. 3(a) and 3(c) are the theoretical calculations, in which a U value of 2.0 eV and a SOC constant of 0.4 eV were used to optimize the calculation for matching to optical conductivity spectra. In the calculations, as the result of strong SOC, the Ir 5d t_{2g} band splits into the effective J_{eff}=1/2 (doublet) and J_{eff}=3/2 (quartet) bands. The near-E_F half-filled J_{eff}=1/2 band further splits into the effective upper and lower Hubbard bands due to its very small effective band width in spite of the relatively small on-site Coulomb repulsion. Here we note that the overall band calculations match the experimentally determined dispersion reasonably well for both materials, with no shifting or scaling of the data. Consistent with the lack of scaling, the intra-cell bilayer splitting observed in the calculation of $Sr_3Ir_2O_7$ (~ 0.25 eV) is also fully consistent with the experiment. This lack of a scaling is surprising for correlated electron materials, which are usually found to have reduced bandwidths (or enhanced masses) relative to the LDA calculations. The lack of a scaling found here may be a result of the relatively small U for these materials. The overall agreement between the band calculation and the experimental dispersion provides additional evidence for this "J_{eff}=1/2 Mott state" picture, and encourages us to follow the theoretical calculation and color code our experimental result with red dashed lines representing the J_{eff}=1/2 bands[21].

Despite the significant agreement between the theory and experiment, important differences remain. In the calculations, the lowest energy occupied states are at Γ (at both Γ and X for Sr_2IrO_4), as highlighted by the red ovals. As seen from the plots of fig. 3, the bilayer splitting at Γ is the reason why $Sr_3Ir_2O_7$ is predicted to have a larger bandwidth and smaller gap than Sr_2IrO_4. In contrast, for the experiment the states at Γ are farther away from the Fermi level, and the states at X will be the most dominant for the low energy properties. Figs. 4(a)-(c) are LDA, LDA+spin-orbit coupling (SOC), and LDA+SOC+U band calculations of Sr_2IrO_4, adopted from B. J. Kim *et al*[8]. Fig. 4(d) is the experimental dispersions of Sr_2IrO_4 obtained by our ARPES measurement. Based on the calculations, the introduction of SOC (~ 0.4 eV) will introduce the splitting of the t_{2g} bands into J_{eff}=1/2 and J_{eff}=3/2 bands. From the calculated dispersions, this splitting is significant at both the Γ and M points, while it is minimal at the X point. At the Γ point, the blue and red bands in panel (a) split into the purple and pink bands in panel (b), with the purple band moving to lower energy. At the M point, the highly degenerate group of bands at -0.5 eV splits, with two of the bands moving towards E_F, as indicated by the up-arrow. The on-site correlation effect (~ 2 eV) further splits these two bands, with the splitting almost uniform in momentum space as shown in panel (c). In an overall picture, from the calculations, the SOC in the system makes the lowest energy electronic state near Γ move downwards (away from E_F) while doing the opposite at the M point. By increasing the SOC strength parameter used in the calculations, we may expect that the calculated lowest energy electronic states near Γ and M will keep moving towards the opposite direction and at a certain level the electronic state near Γ will have a higher binding energies than the state at M (and X). This is exactly what we obtained from the experiment as shown in panel (d). Due to the overall agreement between the band calculations and the experimental dispersions, in panel (d) we color-

coded the experimental dispersions in a similar way as shown in the calculations. It shows that the lowest energy electronic state near Γ has larger binding energy than the state near M, as indicated by the arrows at those two high symmetry points. This is an indirect evidence of the underestimation of the SOC in the calculations. Alternatively, the disagreement in the energy positions of the bands between experiment and theory may be explainable as a strongly momentum-dependent self-energy.

Based on the discussion above, the intra-cell bilayer splitting is not seen to affect the bandwidth in the actual material, and so it is not expected to directly affect the magnitude of the Mott gap. In the calculation, the individual J_{eff}=1/2 bands in Sr_2IrO_4 are positioned at the average energy of the bilayer split J_{eff}=1/2 bands of $Sr_3Ir_2O_7$. Therefore, both materials show the same energy gap at the X point (where the bilayer splitting goes to zero). Another mechanism is therefore needed to explain the difference in the gap size between the two materials. We will show that this is most likely the inter-cell coupling, which we experimentally find to be significantly larger for the bilayer samples. Additionally, we note that in the calculation, the same U is used for both materials. Hence this discrepancy may indicate a reduced correlation effect in bi-layer materials which may be due to the feedback effect, where the extra metallicity in $Sr_3Ir_2O_7$ due to the intra- and inter-cell coupling partially screens the onsite U and results in a reduced correlation effect.

C. Three-dimensional dispersion and connection to transport activation energy

Fig. 5 shows details of the states at the X point (the zone corner of the 2D BZ), including the inter-cell coupling effects. Inter-cell coupling gives rise to a coherent dispersion perpendicular to the planes, which can be accessed by varying the incident photon energy. Such data are shown in figs. 5(a) and 5(b), which are stacks of EDCs at the zone corner with photon

energy varying from 80 eV to 140 eV. Here we find that throughout the large photon energy range, Sr_2IrO_4 always shows a larger energy gap than $Sr_3Ir_2O_7$. Furthermore, for Sr_2IrO_4 the EDCs at the zone corner taken with different photon energies all have a very similar lineshape and peak position. In contrast, for $Sr_3Ir_2O_7$ the EDC lineshapes change a lot as a function of excitation energy and the peak position shows very strong photon energy dependence. Figs. 5(c) and 5(d) summarize the low energy peak positions of Sr_2IrO_4 and $Sr_3Ir_2O_7$ as a function of photon excitation energy. Utilizing the free-electron final-state approximation, we can convert the photon energy to a corresponding k_z value by $k_z = \sqrt{\frac{2m}{\hbar^2}(E_i + h\upsilon - \phi - V_0) - k_{||}{}^2}$ for both Sr_2IrO_4 and $Sr_3Ir_2O_7$, where E_i is the energy of the electron in its initial state (relative to E_F), $h\upsilon$ is the photon excitation energy, ϕ is the sample work function, and V_0 is an experimentally determined inner potential[22]. By fitting the periodicity of the spectra, the inner potentials of -17 $\pm$ 1.4 eV for Sr_2IrO_4 and -25 $\pm$ 0.6 eV for $Sr_3Ir_2O_7$ are obtained, which are large but still within normal range for typical clean surfaces[23]. For Sr_2IrO_4, the experimental result shows the periodicity as $4\pi/c_1$, where $c_1 = 25.8$ Å as the lattice constant in the c direction. This is fully consistent with its tetragonal lattice structure. For $Sr_3Ir_2O_7$, the experimental dispersion shows the periodicity close to $8\pi/c_2$, where $c_2 = 20.9$ Å is its c-axis lattice constant. This extra factor of two in the periodicity is not understood yet. Here we note that the inner potential obtained for $Sr_3Ir_2O_7$ (-25 eV) is larger than that of Sr_2IrO_4 (-17 eV). On one hand, the larger inner potential of $Sr_3Ir_2O_7$ indicates a larger surface dipole potential in $Sr_3Ir_2O_7$, which is in general consistent with the larger valence band width in $Sr_3Ir_2O_7$. On the other hand, an uncertainty of the inner potential of $Sr_3Ir_2O_7$ may also exist due to possible photon energy dependent transition matrix element, as reported in $Sr_3Ru_2O_7$, a similar perovskite 4d-TMO[24]. Nevertheless, by defining the energy gap as the peak-to-E_F distance, we can parameterize the gap size for both materials as the

function of k_z, obtaining $\Delta_{n=1} = 0.287 + 0.004 \cdot \cos(k_z)$ and $\Delta_{n=2} = 0.136 + 0.039 \cdot \cos(k_z)$, both in eV. The black dashed lines in figs. 5(c) and 5(d) represent the fitting results. Here we plot them as a function of excitation energy instead of k_z value since the k_z is essentially a function of photon energy. The high symmetry points along z direction are labeled as Γ and Z for Sr_2IrO_4, and Γ' and Z' for $Sr_3Ir_2O_7$. These data allow us to find the absolute minimum of the peak in the 3D BZ, which is 97 meV from E_F for $Sr_3Ir_2O_7$ and 282 meV from E_F for Sr_2IrO_4. We see that the increased dimensionality in $Sr_3Ir_2O_7$ significantly affects the Mott gap, because the inter-cell k_z dispersion acts directly on the lowest energy states at the X point.

The sharpest leading edge for $Sr_3Ir_2O_7$ is of order 90 meV, and the sharpest edge for Sr_2IrO_4 is more than 180 meV. In both cases this is much larger than the experimental energy resolution, which is at most 35 meV. Therefore, these edge widths and pole energies should have very minimal shifts due to resolution effects, which is confirmed by our simulation also (not shown). On the other hand, the very small but still finite spectral weight observed at E_F in $Sr_3Ir_2O_7$ is within the resolution window of the experiment, i.e. it is possibly fully a result of the finite experimental resolution. Because the pole energy is not affected by the finite energy resolution we can make firm connections between this energy scale and other experimental probes, in particular transport. Within the standard theory of insulators, the electrical resistivity relates to a so-called activation energy E_A through an exponential relation as $\rho \sim \rho_0 \cdot \exp(E_A/k_BT)$ where the activation energy E_A has a value of half of the band gap ($E_A = E_g/2$), and the band gap E_g is the energy difference between the occupied and unoccupied quasiparticle poles. Typically we expect the Fermi energy to be near the center of the band gap – in that approximation the ARPES pole energies would predict resistive activation energies of 282 meV for Sr_2IrO_4 and 97 meV for $Sr_3Ir_2O_7$. These values are much larger than the measured activation

209 energies from transport, which are roughly 105 meV for Sr_2IrO_4[25] and 20 meV for $Sr_3Ir_2O_7$[16,26].
210 Even if we make the most extreme approximation that the unoccupied pole is exactly at the
211 chemical potential (which would then give a clear signal in the occupied ARPES spectral weight)
212 we predict activation energies of 141 meV for Sr_2IrO_4 and 48 meV for $Sr_3Ir_2O_7$, which are
213 between 40% and 150% larger than the actual value from transport. This disagreement is
214 highlighted in figs. 5(e) and 5(f), where the experimental activation energies are plotted on top of
215 the ARPES data. As just discussed, these differences are so large that they can't be due to the
216 possible uncertainty of the Fermi energy location within the band gap, but rather must be due to a
217 fundamental breakdown of the simple picture that relates the pole energies to the activation
218 energies. Rather, the data of figs. 5(d) and 5(e) indicate that the activation energy is related to the
219 onset of the spectral weight of the pole, rather than the pole energy itself. Though such a direct
220 comparison to activation energies has not to our knowledge been made before, such behavior has
221 been observed in other correlated electron systems, for example the manganites[27] or cuprates[28]
222 where the peak energy is observed to be far from E_F, argued in both cases to be the result of
223 correlation effects (in particular polaronic effects). Such a distinction of course only makes sense
224 for a correlated electron insulator with a finite peak width, as a standard insulator should have
225 vanishingly small peak width for the low energy peak in the low temperature limit (in the same
226 way that the low temperature quasiparticle width of a Fermi liquid metal goes to zero at E_F). The
227 fact that the less correlated $Sr_3Ir_2O_7$ has a smaller peak width than the more correlated Sr_2IrO_4 is
228 also consistent with this behavior. This behavior is also fully consistent with J_{eff}=1/2 Mott
229 ground state picture, in which the relatively small on-site Coulomb repulsion will lead to a split
230 of the near-E_F half-filled J_{eff}=1/2 band due to its very small effective band width, and the near E_F
231 excitation of both Sr_2IrO_4 and $Sr_3Ir_2O_7$ should be described by Mott physics instead of the

quasiparticle picture.

Going beyond $Sr_3Ir_2O_7$, we envision that a further increase in the dimensionality could bring about a further reduction in the gap energies such that the edges of the spectral peaks could overlap with E_F while the peak centroids remain away from E_F. Such a metal, where the spectral peaks potentially never reach the Fermi energy, would have analogies to the famous pseudogap states in the manganites and cuprates, further cementing the similarities between different classes of Mott insulators on the verge of metallicity.

IV. CONCLUSIONS

In summary, by using ARPES, we studied the electronic structure of single- and bi-layer perovskite iridates Sr_2IrO_4 and $Sr_3Ir_2O_7$. The overall electronic structures of both materials are partially consistent with the LDA+U+SOC calculations based on the J_{eff}=1/2 Mott ground state picture, though the calculations also miss some critical physics. The different dimensionality between these two materials, in particular, the strong intercell coupling in $Sr_3Ir_2O_7$ makes it have less Mottness with smaller energy gap, sharper peaks, and larger k_z dispersion comparing to Sr_2IrO_4.

ACKNOWLEDGMENTS

This work was supported by the National Science Foundation under grant DMR-1007014 to the University of Colorado and grants DMR-0856234 and EPS-0814194 to the University of Kentucky. This work is also based in part upon research conducted at the Advanced Light Source, which is funded by the US Department of Energy, and at the Synchrotron Radiation Center

which is primarily funded by the University of Wisconsin-Madison with supplemental support from the University of Wisconsin-Milwaukee.

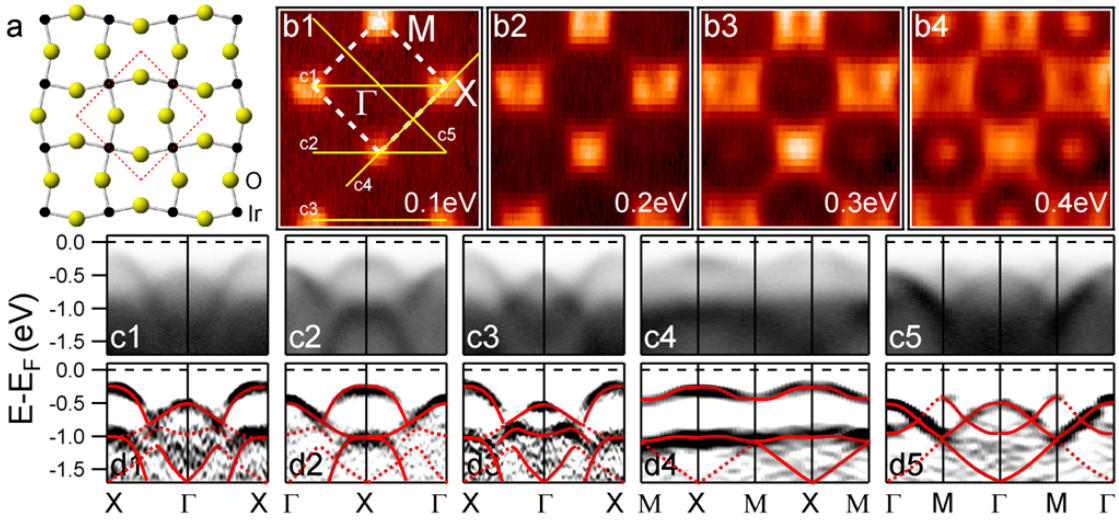

FIG. 1: (a) In-plane crystal structure of Sr_2IrO_4. The red dashed box represents the in-plane unit cell. (b1-b4) Intensity maps at different binding energies from 0.1 eV to 0.4 eV of Sr_2IrO_4. (c1-c5) Spectra taken along high symmetry cuts c1 to c5 as indicated by the yellow lines in panel (b1). (d1-d5) Second-derivative images along energy direction of spectra c1-c5, respectively. The red solid and dashed lines are guides for the eyes of the experimental observed dispersion. All data were taken with 80 eV photons at 25 K.

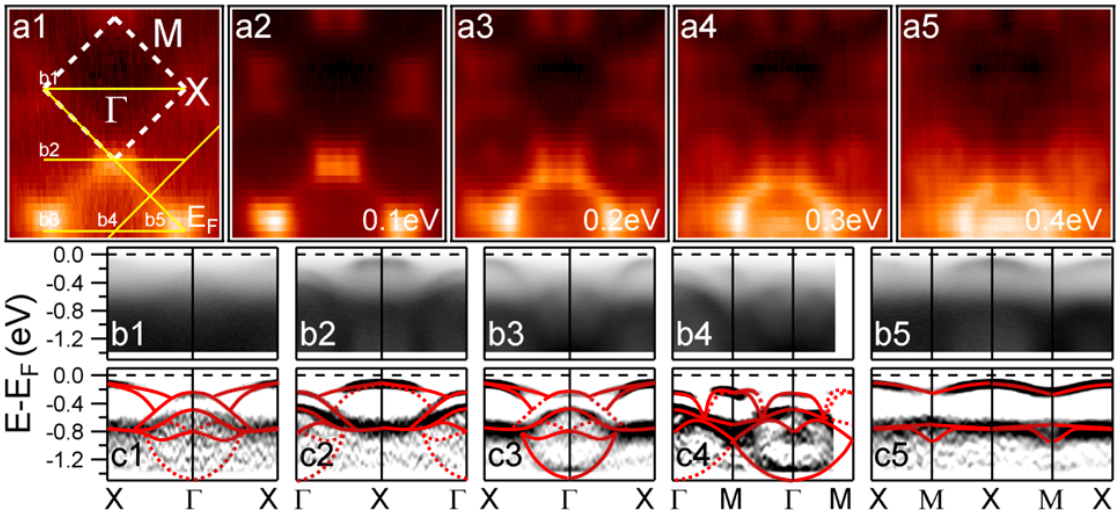

FIG. 2: (a1-a5) Intensity maps at different binding energies from Fermi level to 0.4 eV of $Sr_3Ir_2O_7$. (b1-b5) Spectra taken along high symmetry cuts b1 to b5 as indicated by the yellow lines in panel (a1). (c1-c5) Second-derivative images along energy direction of spectra b1-b5, respectively. The red solid and dashed lines are guides for the eyes of the experimental observed dispersion. All data were taken with 80 eV photons at 25 K.

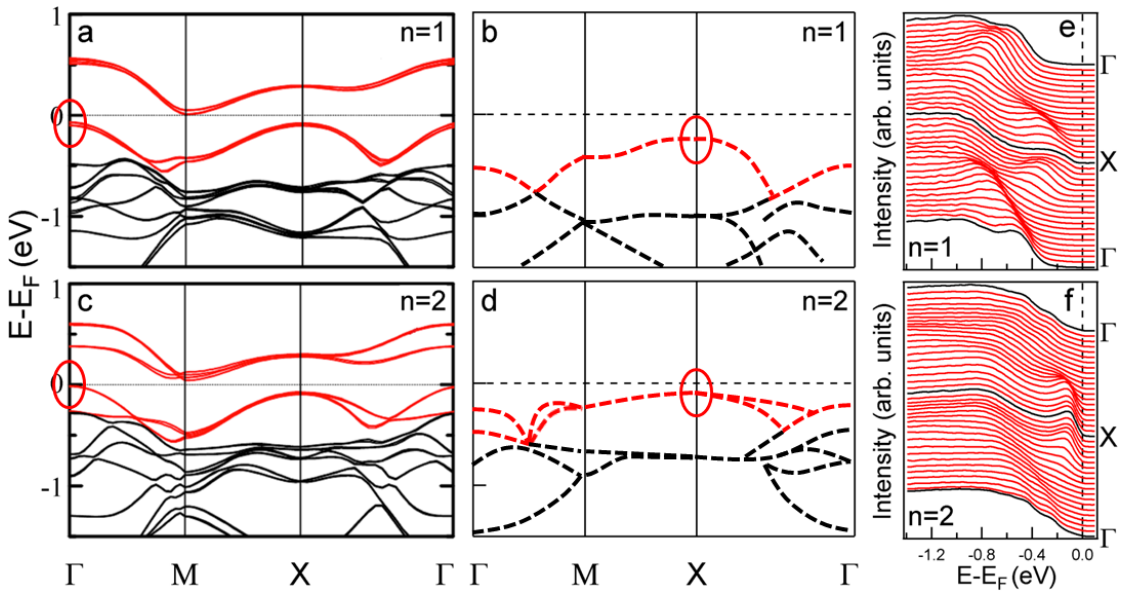

FIG. 3: (a,c) LDA+U+SOC band calculations of Sr_2IrO_4 (top) and $Sr_3Ir_2O_7$ (bottom), adopted from S. J. Moon *et al*[9]. (b,d) Experimental dispersions (centroids of spectral weight) of Sr_2IrO_4 (top) and $Sr_3Ir_2O_7$ (bottom). The red and black lines represent the J_{eff}=1/2 and J_{eff}=3/2 bands, respectively. In the calculations, the dominant low energy occupied states are at the Γ point (red ovals). In the experiment, the dominant low energy states are at the X point (red ovals) instead. (e) and (f) Stacks of EDCs along the Γ-X-Γ directions for Sr_2IrO_4 (top) and $Sr_3Ir_2O_7$ (bottom).

267

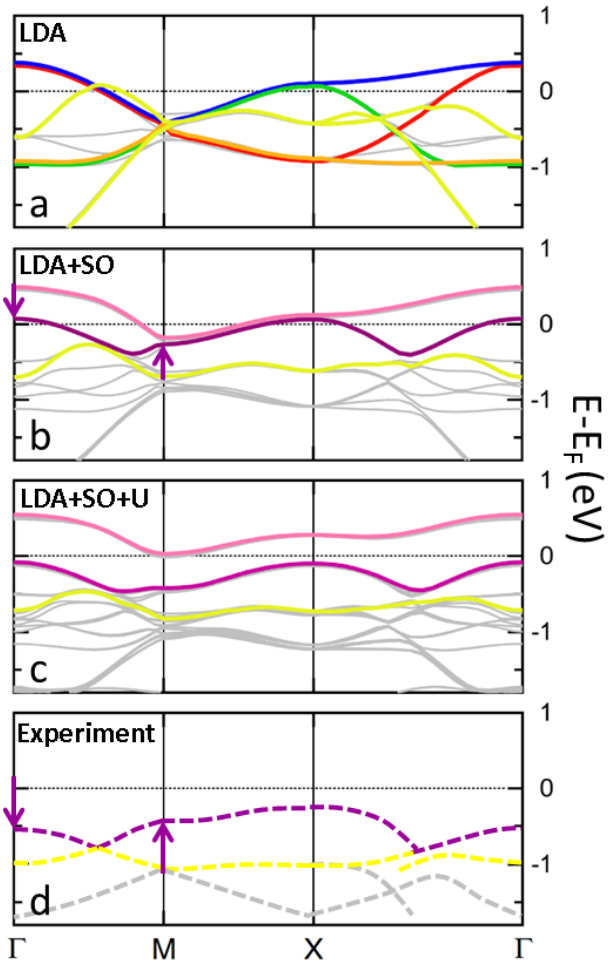

FIG. 4: Comparison between the experimental dispersions and the theoretical calculations of Sr_2IrO_4. Theoretical band dispersions of Sr_2IrO_4 in (a) LDA, (b) LDA+SOC (~ 0.4 eV), (c) LDA+SOC+U (~ 2 eV), adopted from B. J. Kim *et al*[8]. (d) Proposed experimental dispersions of Sr_2IrO_4 for comparison. The vertical arrows in panel (b) show the clear impact of SOC on the band structure, which raises the low energy state at M and lowers it at Γ. As shown by the longer arrows in panel (d), the experimental data follows a trend that may be explainable with a still larger value of SOC.

268

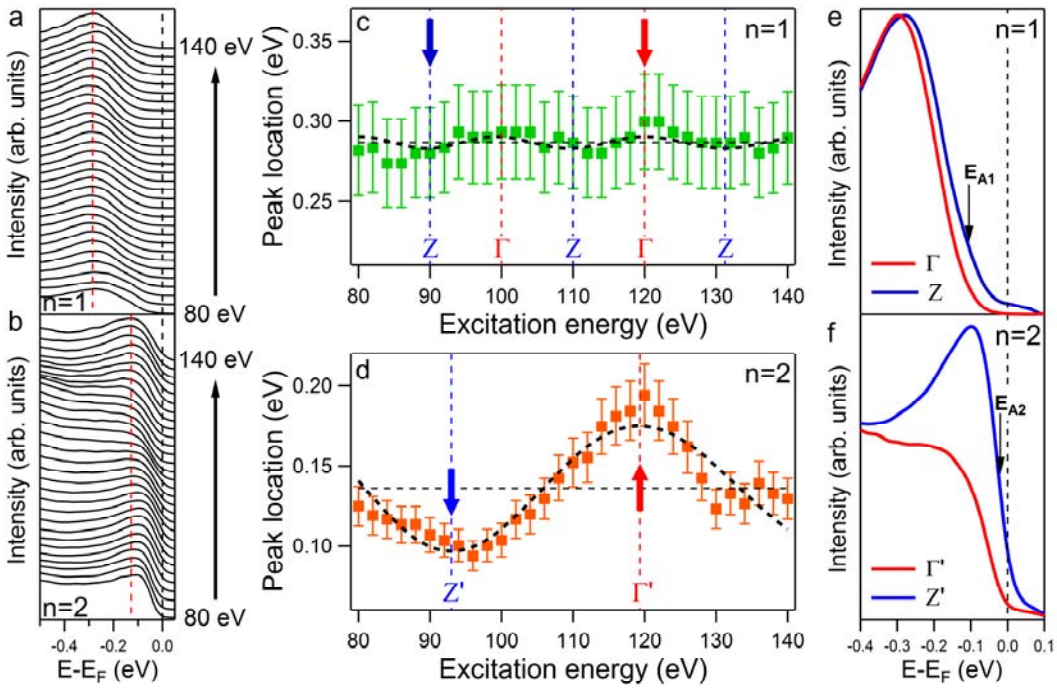

FIG. 5: (a) and (b) Photon energy dependence of the EDCs at the X point for Sr_2IrO_4 and $Sr_3Ir_2O_7$ (80 eV to 140 eV with 2 eV/step). The red dashed lines are guide to the eyes for viewing the variation of the EDC peak locations. (c) and (d) Extracted peak energy as a function of excitation energy for Sr_2IrO_4 and $Sr_3Ir_2O_7$, respectively. The black dashed curves in (c) and (d) are fitted curves obtained by fitting the peak energy with the function $\Delta = \Delta_0 + \eta \cdot \cos(k_z)$, where $k_z = \sqrt{\frac{2m}{\hbar^2}(E_i + h\upsilon - \phi - V_0) - k_{||}{}^2}$. The Γ and Z labeled in (c), and the Γ' and Z' labeled in (d) indicate the high symmetry points in k_z direction of Sr_2IrO_4 and $Sr_3Ir_2O_7$, respectively. (e) and (f) EDCs at Γ and Z for Sr_2IrO_4, at Γ' and Z' for $Sr_3Ir_2O_7$, indicated by red and blue arrows in panel (c) and (d), respectively. The black arrows indicate the measured activation energies from transport for Sr_2IrO_4 (E_{A1}=105 meV) and $Sr_3Ir_2O_7$ (E_{A2}=20 meV).

269

[1] J. G. Bednorz, and K. A. Müller, *Z. Phys. B* **64**, 189-193 (1986).

[2] F. Wang, and T. Senthil, *Phys. Rev. Lett.* **106**, 136402 (2011).

[3] A. Shitade, H. Katsura, J. Kuneš, X.-L. Qi, S.-C. Zhang, and N. Nagaosa, *Phys. Rev. Lett.* **102**, 256403 (2009).

[4] B. J. Yang, and Y. B. Kim, *Phys. Rev. B* **82**, 085111 (2010).

[5] H. C. Jiang, Z. C. Gu, X. L. Qi, and S. Trebst, *Phys. Rev. B* **83**, 245104 (2011).

[6] C. H. Kim, H. S. Kim, H. Jeong, H. Jin, and J. Yu, *Phys. Rev. Lett.* **108**, 106401 (2012).

[7] X. G. Wan, A. M. Turner, A. Vishwanath, and S. Y. Savrasov, *Phys. Rev. B* **83**, 205101 (2011).

[8] B. J. Kim, H. Jin, S. J. Moon, J.-Y. Kim, B.-G. Park, C. S. Leem, J. Yu, T. W. Noh, C. Kim, S.-J. Oh, J.-H. Park, V. Durairaj, G. Cao, and E. Rotenberg, *Phys. Rev. Lett.* **101**, 076402 (2008).

[9] S. J. Moon, H. Jin, K. W. Kim, W. S. Choi, Y. S. Lee, J. Yu, G. Cao, A. Sumi, H. Funakubo, C. Bernhard, and T. W. Noh1, *Phys. Rev. Lett.* **101**, 226402 (2008).

[10] B. J. Kim, H. Ohsumi, T. Komesu, S. Sakai, T. Morita, H. Takagi, T. Arima, *Science* **323**, 1329 (2009).

[11] H. Jin, H. Jeong, T. Ozaki, and J. Yu, *Phys. Rev. B* **80**, 075112 (2009).

[12] H. Watanabe, T. Shirakawa, and S. Yunoki, *Phys. Rev. Lett.* **105**, 216410 (2010).

[13] K. Ishii, I. Jarrige, M. Yoshida, K. Ikeuchi, J. Mizuki, K. Ohashi, T. Takayama, J. Matsuno, and H. Takagi, *Phys. Rev. B* **83**, 115121 (2011).

[14] R. Arita, J. Kunes, A. V. Kozhevnikov, A. G. Eguiluz, and M. Imada, *Phys. Rev. Lett.* **108**, 086403 (2012).

[15] G. Cao, J. Bolivar, S. McCall, J. E. Crow, and R. P. Guertin, *Phys. Rev. B* **57**, R11039 (1998).

[16] G. Cao, Y. Xin, C. S. Alexander, J. E. Crow, P. Schlottmann, M. K. Crawford, R. L. Harlow, and W. Marshall, *Phys. Rev. B* **66**, 214412 (2002).

[17] M. K. Crawford, M. A. Subramanian, R. L. Harlow, J. A. Fernandez-Baca, Z. R. Wang, and D. C. Johnston, *Phys. Rev. B* **49**, 9198 (1994).

[18] Q. Huang, J. L. Soubeyroux, O. Chmaissem, I. Natali Sora, A. Santoro, R. J. Cava, J. J. Krajewski, and W.F. Peck Jr., *J. Solid State Chem.* **112**, 355 (1994).

[19] Z.-X. Shen, and D. S. Dessau, *Phys. Rep.* **253**, 1-162 (1995).

[20] A. Damascelli, Z. Hussain, and Z.-X. Shen, *Rev. Mod. Phys.* **75**, 473-541 (2003).

[21] There is still some theoretical uncertainty over the nature of the states near the Γ point. In particular, the calculations done by Watanabe *et al*. indicated that the J_{eff}=1/2 and J_{eff}=3/2 states cross near the Γ point so that the J_{eff}=3/2 states are closer to E_F[12]. Further efforts are required to clarify the exact nature of these states.

[22] S. Hüfner, *Photoelectron Spectroscopy* (Springer, 1995).

[23] C. S. Fadley, Progress in Surface Science ***16***, 275 (1984).

[24] A. V. Puchkov, Z.-X. Shen, and G. Cao, *Phys. Rev. B* **58**, 6671 (1998).

[25] M. Ge, T. F. Qi, O. B. Korneta, D. E. De Long, P. Schlottmann, W. P. Crummett, and G. Cao, *Phys. Rev. B* **84**, 100402(R) (2011).

[26] The transport data presented in ref. 16 was refitted within temperature range 250-350 K and a 23.6 meV activation energy was obtained for $Sr_3Ir_2O_7$.

[27] D. S. Dessau, T. Saitoh, C.-H. Park, Z.-X. Shen, P. Villella, N. Hamada, Y. Moritomo, and Y. Tokura, *Phys. Rev. Lett.* **81**, 192 (1998).

[28] Kyle M. Shen, F. Ronning, D. H. Lu, F. Baumberger, N. J. C. Ingle, W. S. Lee, W. Meevasana, Y. Kohsaka, M. Azuma, M. Takano, H. Takagi, Z.-X. Shen, *Science* **307**, 901 (2005).